京 都 大 学 防 災 研 究 所 年 報　第48号 C　平成17年4月
Annuals of Disas. Prev. Res. Inst., Kyoto Univ., No. 48 C, 2005

Advanced Techniques for Evaluating Vulnerability of Urban Infrastructure by Integrating Multiple Evaluation Indexes

Tadanobu SATO, Hitoshi TANAKA, Masayoshi NAKASHIMA, Tomotaka IWATA,
Keiichiro SUITA, Sumio SAWADA, Shuji TAMURA,
Riki HONDA, Nobuyuki YAMADA*

* Disaster prevention Research Institute, Kyoto University

Synopsis

It is essential for disaster prevention to quantitatively evaluate the earthquake vulnerability of urban infrastructures considering the duration of infrastructures in service, external loads to act on structure during earthquakes, cost of damage and restoration, and the cost of maintenance and retrofitting. For this purpose, we propose an integrated methodology that covers the prediction of strong ground motions for scenario earthquakes, a full-scale test of a frame sub-assemblage including RC floor slabs, concrete members reinforced by newly developed polyacetal-fiber (PAF) filaments, the horizontal subgrade reaction of foundation piles during soil liquefaction and an efficient method to estimate a fragility curve based on Subset Simulation method and MCMC (Markov Chain Monte Carlo).

Keywords: strong ground motion prediction, long period ground motions, seismic rehabilitation, full-scale experiment, life cycle cost, fragility curve

1. Introduction

To evaluate earthquake vulnerability of urban infrastructures we have to develop techniques for evaluating (1) life time of infrastructures, (2) external input to structure during event occurrences, (3) cost of damage to infrastructures and restoration cost, (4) maintenance and retrofit cost. For this purpose we are conducting researches on prediction of strong ground motions for scenario earthquakes, a full-scale test of a frame sub-assemblage including RC floor slabs, concrete members reinforced by newly developed polyacetal-fiber (PAF) filaments, the horizontal subgrade reaction of foundation piles during soil liquefaction and an efficient method to estimate a fragility curve based on Subset Simulation method and MCMC (Markov Chain Monte Carlo).

In the next chapter, we are constructing a framework of strong ground motion prediction using a characterized source model and underground structure model for scenario earthquakes. The observed ground motion during 2004 off the Kii-Peninsula earthquake is used for validating the underground structure model Simulated long-period ground motions fairly well reproduced the observation and that model is applicable for long-period ground motion simulation of coming Tonankai and Nankai earthquakes.

In the third chapter, a full-scale test of a frame sub-assemblage including RC floor slabs was conducted to obtain realistic data about the performance of composite beams in deformation ranges much larger than those considered in seismic design. Finite element analysis was also conducted to simulate progressive collapse of composite systems. We propose a model that is capable of capturing the behavior of test structure before and after the connection fracture with acceptable accuracy.

In the forth chapter, the strengthening effects of

reinforced concrete members by applying newly developed polyacetal-fiber (PAF) filaments was investigated. In addition, the horizontal subgrade reaction of foundation piles during soil liquefaction has also been studied.

The necessity of effective method to estimate low failure probability is increased from the standpoint of evaluation of life cycle cost, risk and probabilistic safety assessment (PSA). In the last chapter, We propose an efficient method to estimate a fragility curve by using Monte Carlo simulation and limit seismic intensity, which is defined as the minimum amplitude of input motion causing damage to a structure. When the uncertainty of seismic load is not so large, the tail part of the fragility curve is important to estimate failure probability accurately. For the effective estimation of the tail part, namely low conditional failure probability, we use Subset Simulation method. Samples are generated to search the failure region in each subspace by using MCMC (Markov Chain Monte Carlo). The proposed method is verified through a numerical example with simple limit state functions, and then a fragility curve of a steel pier of bridge is calculated by the proposed method.

2. Strong Ground Motion Prediction for Design Ground Motion

The M8-class subduction earthquakes have occurred repeatedly in Nankai trough. The headquarters for earthquake research promotion reported that long-term evaluations of occurrence potentials of the next Nankai and Tonankai earthquakes at the trough are from 50% to 60% within 30 years from 2005. During the 2003 Tokachi-Oki earthquake (MJ8.0), many oil tanks in Tomakomai city, about 250km far from the source region, were damaged by long-period ground motions. Long-period ground motion is generated by large earthquake and large sedimentary basin effects. This shows that long-period ground motions attack Osaka, Nobi, and Kanto sedimentary basins during the Nankai and Tonankai earthquakes.

Two large earthquakes with MJ 7.1 and 7.4 rocked Honshu from Kanto to Kyushu on September 5, 2004. These events occurred off Kii peninsula in the shallower part of the subducting Philippine Sea plate. Although these events did not occur source regions of the hypothetical Tonankai earthquake, strong motion records including long-period ground motions were observed. Sufficient-quality ground motion data in the wide period range from these events enable us to confirm the validity of the underground structure model for long-period ground motion simulation. Here, we show the characteristics of observed long-period ground motions and try to simulate long-period ground motions in Kinki area to validate the underground structure model.

2.1 Long-period ground motion characteristics of the 2004 off the Kii-Peninsula earthquake

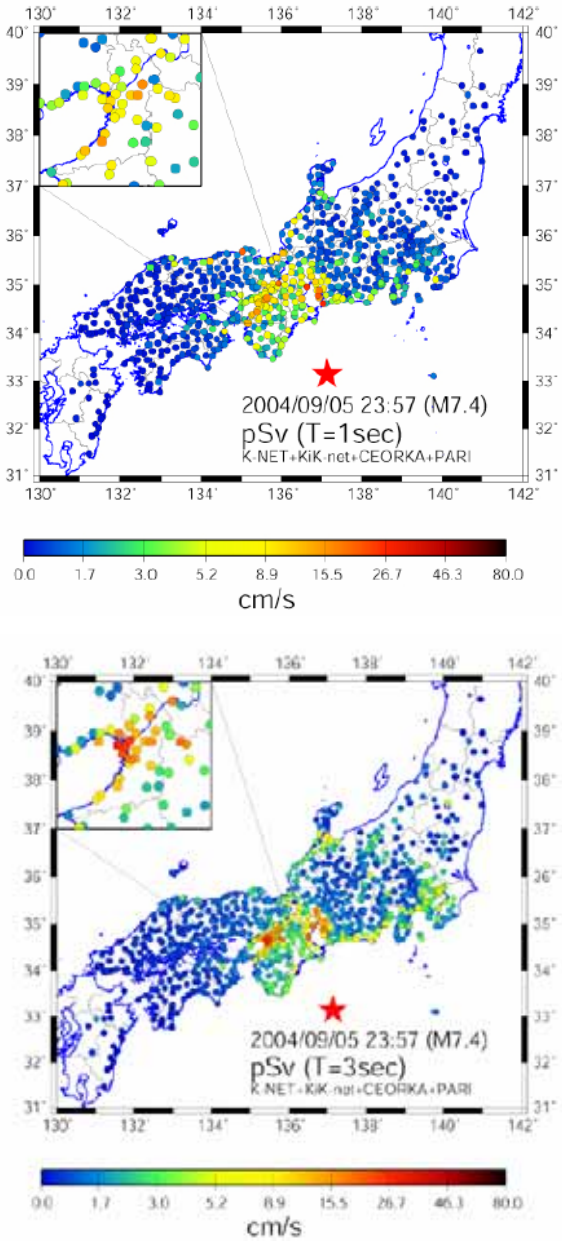

Fig.1 Distribution of pseudo velocity response spectra during the mainshock. (5%, 1s and 3s)

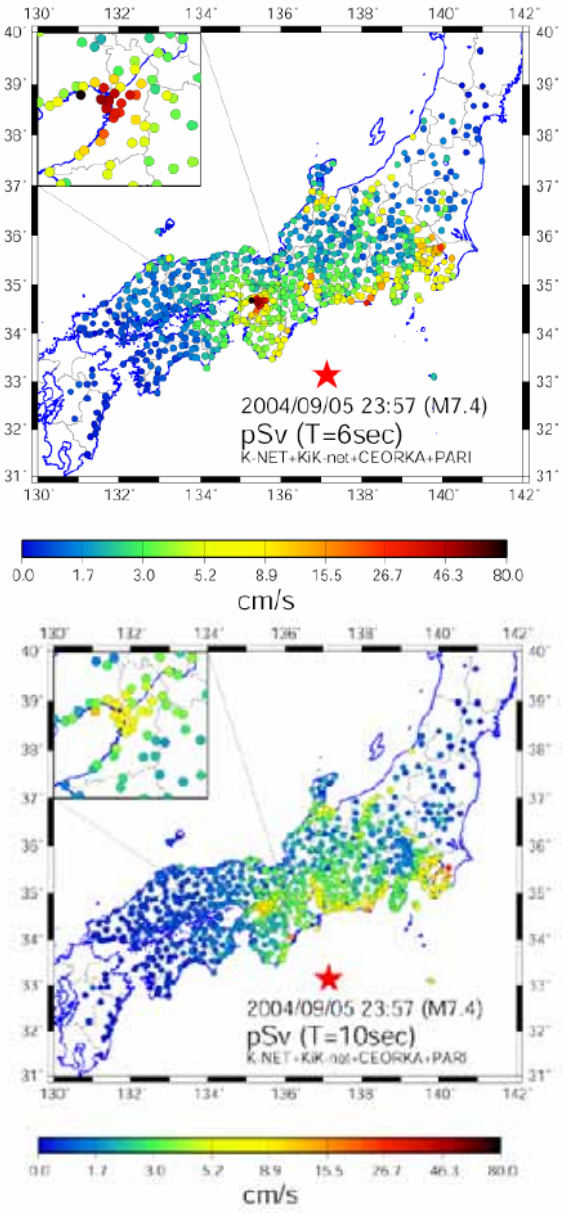

Fig.1(continued) Distribution of pseudo velocity response spectra during the mainshock. (5%, 6s and 10s)

Fig.1 shows distribution of pseudo velocity response spectra (larger horizontal component, damping=5%) during the mainshock. We show those of period of 1, 3, 6, and 10s. At the period of 3s, large responses are observed in Osaka and Nobi basins. At the 6s, coastal area in Osaka basin has maximum response. On the contrary, at the 10s, maximum responses are observed at Kanto coastal area. These characteristics are thought to be occurred by effects of propagation-path and underground structure of the basins. For example, roughly speaking, basin depth and shape of basins would control the predominant period and duration of long period ground motions. To explain the characteristics of long period ground motions, we try to simulate long period ground motions by the source and underground structure model.

2.2 Simulation of long-period ground motions

Fig. 2 shows example of observed ground motion at the rock sites in Kinki area for the pre-event (MJ7.1). Even nearest site to the epicenter, SNM, long duration ground motion is recorded, even the source time duration is about 15s by waveform inversion result (Yagi, 2004). This means that underground structure between source region to the SNM station is complex and modeling of underground structure of this portion is very important for successful simulation of this event records. Fig.3 shows our model area. Osaka, Kyoto, and Nara basins and some portion of Nobi basin are included. Schematic cross section of the model is shown in Fig. 4. The cross section line AA', that includes the source and the Osaka basin, is marked in Fig. 3. In Fig. 4, the source region of the Tonankai earthquake, that is the boundary between the subducting plate and the continental

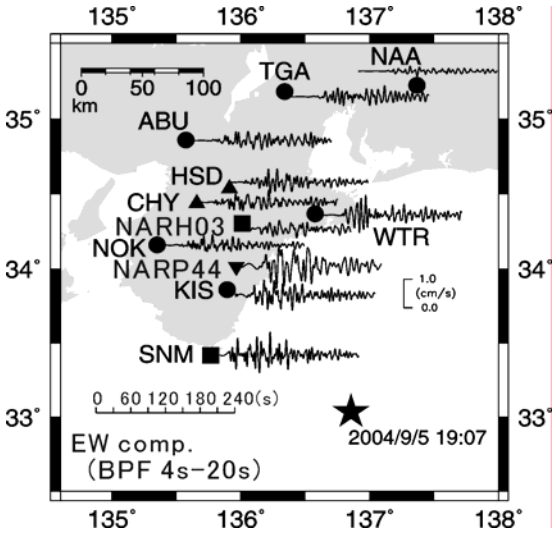

Fig.2 Examples of observed ground velocities (EW component, 4-20s band-pass-filtered).

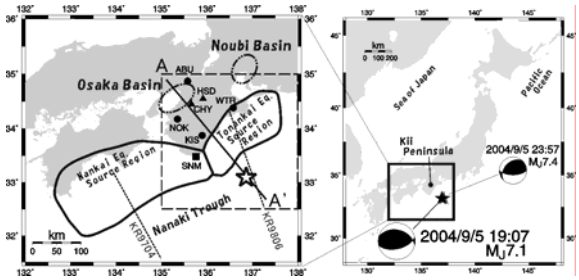

Fig.3 Model area

plate, is also shown. There are sedimentary wedge at subsurface portion between the Kii peninsula and the hypocenter. This sedimentary underground structure would affect to elongate ground motions at the rock sites in the Kii peninsula.

Following to the studies (e.g. Kagawa et al., 2002; Nakamura *et al*, 1997, Zhao *et al.,* 1994, Furumura *et al,* 2003, Yamada and Iwata, 2004) three dimensional velocity structure is constructed. Several interface depth contour maps are shown in Fig. 5. Layer number can be referred to Fig. 4. Source time function consists two continuous triangles whose length is totally 15s, referring to Yagi (2004). In Fig. 6, comparisons between observed and simulated velocity ground motions are shown. All traces are band-pass-filtered to 4-20s. Duration and apparent

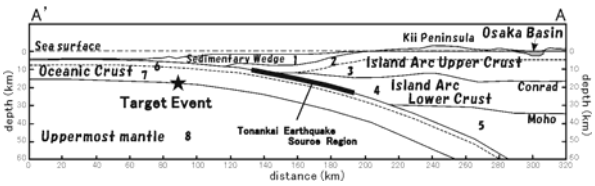

Fig.4 Schematic cross section of the underground structure.

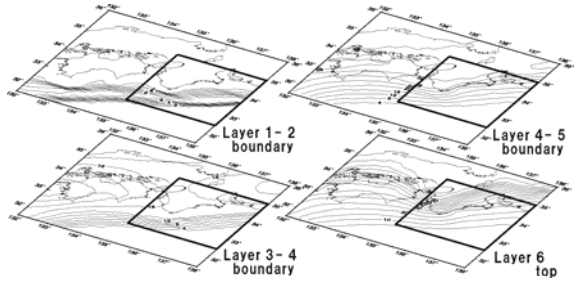

Fig.5 Depth contour map of interfaces of our underground structure model.

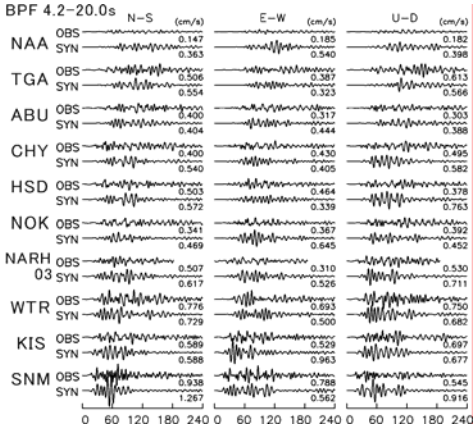

Fig.6 Comparisons of observed and simulated ground velocities.

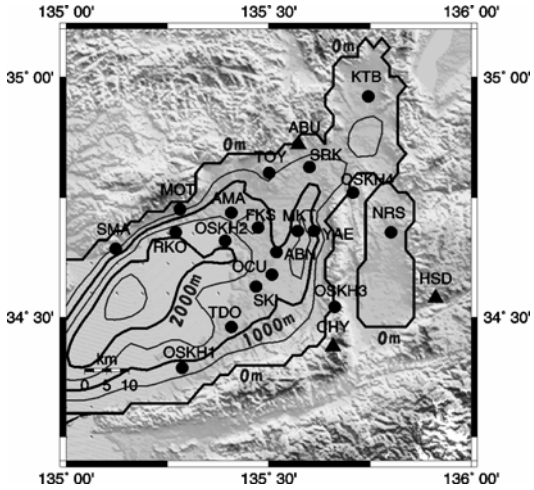

Fig.7 Basin depth in Kansai area.

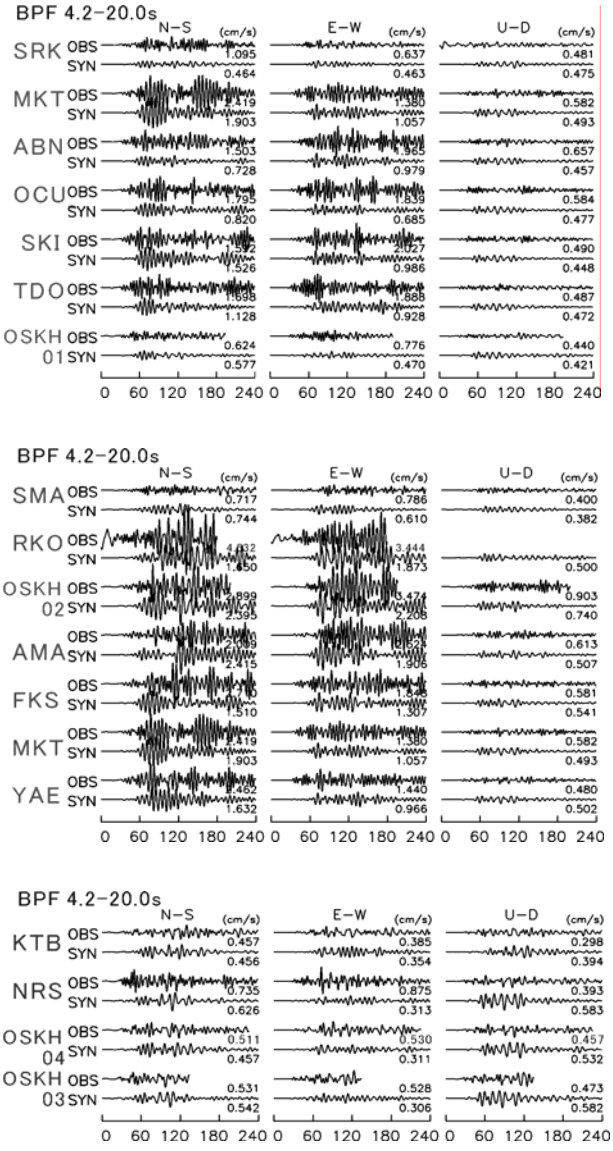

Fig.8 Comparisons between observed and simulated ground velocities at the basin sites.

predominant periods of ground motions are reproduced well.

In Fig. 7, basin depth map in the Osaka, Kyoto, and Nara region is shown. Comparisons between observed and simulated velocity ground motions are shown in Fig. 8. Stations are shown in Fig. 7. Grossly speaking, simulated ground motions fairly well reproduced ground motion duration and amplifications at the sediment stations.

Ground motions for the pre-event of the 2004 Off Kii peninsula earthquake are fairly simulated both at the propagation path and basin sites. Grossly speaking, the constructed underground structure model can be used for long period ground motion simulation in this area. However, insufficient estimations are occurred at several basin sites, and to tune up the model is still needed.

3. Effect of composite action on reserved capacity of steel building structures

3.1 Introduction

In common construction of steel buildings, RC floor slab is always present. According to current design specifications on composite structures, stiffness as well as strength of steel beam increase due to the effects of RC floor slab (composite action).

To ensure life safety by the avoidance of structural collapse under extremely large earthquakes, it is imperative to characterize complete failure of structural members and systems. This involves the investigation into the effects of composite action on complete failure of steel beams. To this end, a full-scale test of a frame sub-assemblage including RC floor slabs was conducted to obtain realistic data about the performance of composite beams in deformation ranges that are far beyond those considered in contemporary seismic design. Finite element analysis was also conducted to simulate progressive collapse of composite systems.

3.2 Test program

The test structure was a two-story, two-bay by one-bay steel moment frame. To ensure that plastic hinges form at beam-ends, relatively strong cross sections were used for columns. Plans and elevations are shown in Fig. 9. Two parallel planar frames placed in the longitudinal direction (Fig. 9) are nearly identical, but one frame (referred to as the composite frame) has a floor slab extending by 1.75 m in the transverse direction on both sides of the beam, while the other frame (referred to as the bare steel frame) has no floor slab. This arrangement was deliberately adopted to directly evaluate the effects of RC floor slab from the difference in resistance between the two frames. The structure was a typical low-rise building designed following the post-Kobe

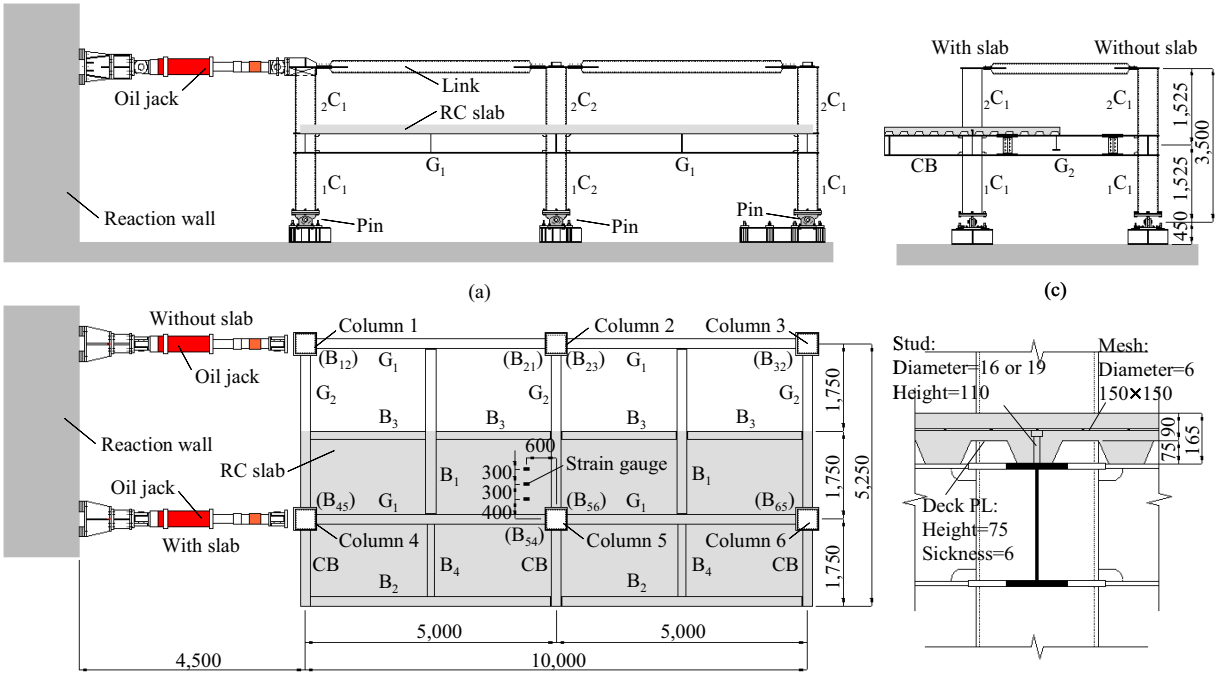

Fig.9 Test specimen: (a) South Elevation; (b) Plan (numbering of beam-ends shown in parentheses); (c) East elevation; (d) Profile of RC floor slab; (unit: mm)

Comparison for local behavior

Japanese seismic design method for steel moment frames.

As shown in Fig. 9, braces were joined horizontally to the column tops by high strength bolts through gusset plates. Two quasi-static jacks were arranged for horizontal loading. Each jack was placed at one end of each frame. An identical displacement was applied by both jacks. Quasi-static cyclic loading with increasing displacement amplitudes was adopted. The displacement was expressed in terms of the overall drift angle, defined as the horizontal displacement at the loading point relative to the loading height (i.e. 3.5 m). Overall drift angles of 0.005, 0.01, 0.015, 0.02, 0.04, 0.06 and 0.1 rad were adopted. Three cycles were repeated for each amplitude except for amplitude of 0.1 rad, in which only one cycle was loaded. The structure was finally pushed up to an amplitude of 0.13 rad, which corresponded the maximum stroke of the jacks.

3.3 Test results

Fig. 10 shows the base shear versus total drift angle relationships for the bare steel frame and composite frame. The base shear was obtained from the load applied by the corresponding jack. Fig. 10(a)-(b) are the plots of loading to the amplitudes of 0.06 rad, whereas Fig. 13(c)-(d) are those plotting the data to 0.13 rad. Although somewhat subjective, 0.06 rad was chosen as the maximum rotation that steel moment frames may experience under large earthquake loads considered in contemporary seismic design. Drift angles greater than 0.06 rad were used for the evaluation of reserved capacity to collapse.

As shown in Fig. 10, the bare steel frame exhibits very stable behavior until the negative loading of the first cycle at 0.06 rad drift angle when the first fracture [refer to ▲ in Fig. 13 (a)] occurred on the bottom flange of beam-end B32 [see Fig.9(b)]. The composite frame also shows stable behavior till the third cycle of positive loading at 0.04 rad drift angle when the first fracture [refer to ▼ in Fig. 13 (b)] developed on the bottom flange of beam-end B45 [see Fig. 9(b)]. All fractures exhibited a brittle mode. The first fracture occurred earlier in the composite beam relative to the bare steel beam. Obviously, the presence of RC floor slab increased the strain demanding of bottom flange, leading to the advance of fracture. As evidenced from Fig. 13(a)-(b), the maximal strength of composite frame is 38% (positive) and 29% (negative) greater than that of the bare steel frame. The effect of RC slab is significant. After the loading of 0.06 rad, all four connections of composite frame failed by the fracture of bottom flanges. All four connections of the bare steel frame failed after the deformation range of 0.1 rad.

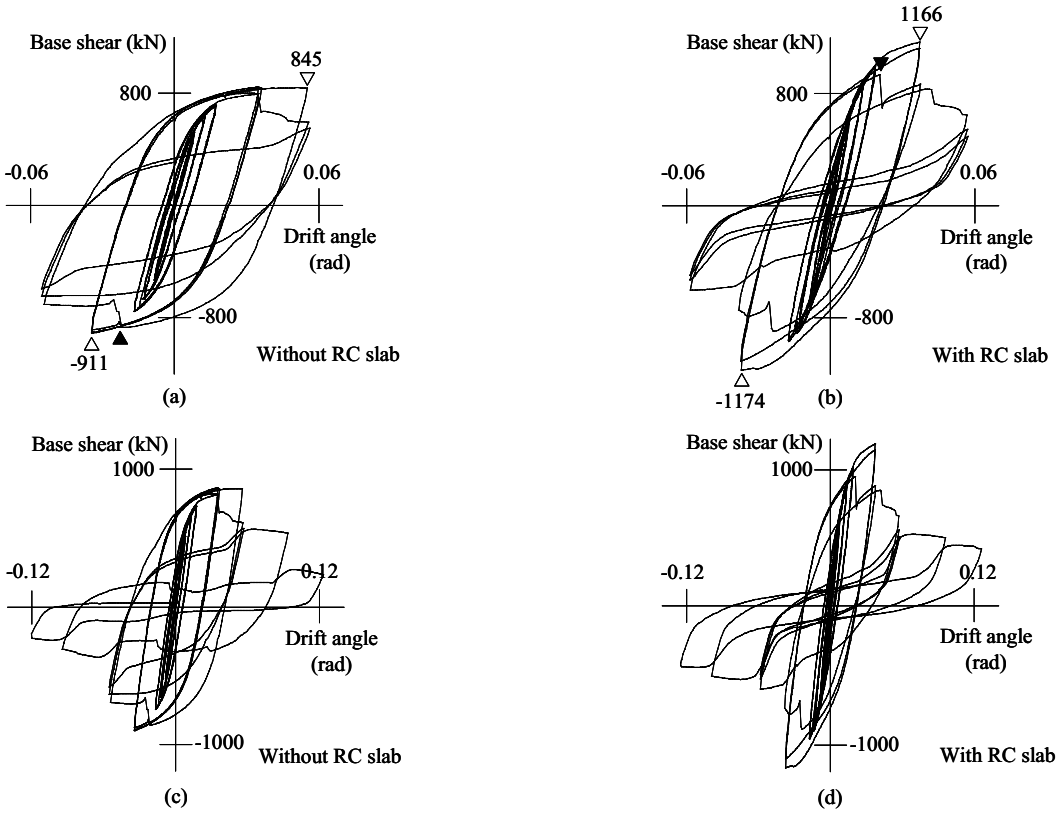

Fig.10 Global performance of each frame: (a) bare steel frame (to 0.06 rad); (b) composite frame (to 0.06 rad); (c) bare steel frame (to 0.13 rad); (d) composite frame (to 0.13 rad)

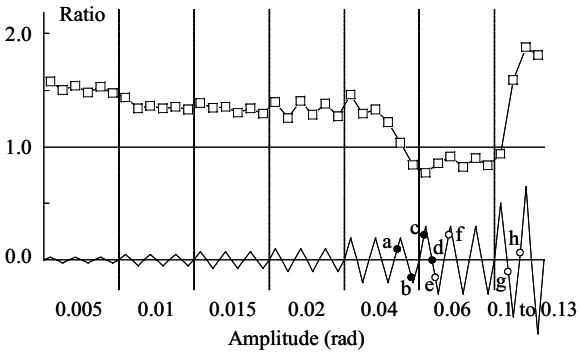

Fig. 11 Comparison of maximal strength

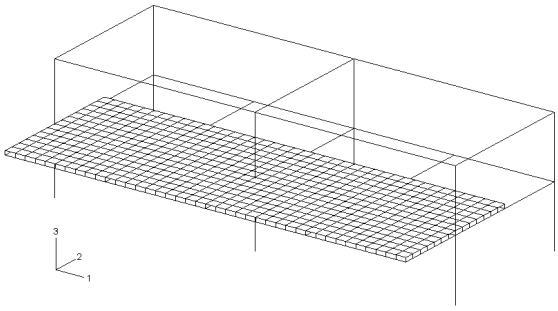

Fig. 12 FE model of test structure

All fractures occurred in the bottom flanges also in the bare steel frame.

The ultimate strength of the composite and bare steel frames for both positive and negative loading are compared in Fig. 11 with respect to the loading amplitude. Symbols, ● and ○, indicate the points of beam bottom flange fracture for the composite or bare steel frames, respectively. As evidenced from Fig. 11, the strength of the composite frame is significantly greater than those of the bare steel frame until the second cycle in the 0.04 rad amplitude at which the first beam fracture occurred in the composite frame. In the 0.005 rad amplitude, which is considered as the deformation level in small to moderate earthquakes, the strength ratio is about 1.5. For the amplitudes exceeding 0.005, the structure was no longer in the elastic range and cracks developed on the RC floor slab. The strength ratio was reduced to about 1.25. After the first fracture in the composite beam (during the positive loading of the third cycle in the 0.04 rad amplitude), the two frames had no difference in the property. After the third fracture in the composite beam (during the positive loading of the first cycle in the 0.06 rad amplitude), the composite frame was smaller in the properties than the bare steel frame, which had not experienced any fracture. The strength of the composite frame is 80% of those of the bare steel frame. In the 0.06 rad amplitude, the ratio remains lower than unity. The ratio of strength drastically increased in amplitudes beyond 0.1 rad when all connections fractured by the fractures of the last two connections that had survived in the bare steel frame. The residual strength of bare steel frame was achieved through the negative bending connections where the separated bottom flange contacted the column faces. While the residual strength of composite frame was achieved through both negative bending connections and positive bending connections in which compressive and tensile forces were sustained by concrete slab and beam top flange. Composite floor slab beneficially maintained the strength of composite frame.

3.4 Modeling of test structure

A general-purpose commercial FE package DIANA 8.1 was adopted to develop the numerical models. To faithfully reproduce all the complicated boundary conditions, the entire test structure including two frames was considered. The FE models are shown in Fig. 12.

The steel beams and columns shown in Fig. 12 are modeled using two-node straight beam elements based on the Bernoulli theory. The RC floor slab with profiled sheet is modeled by four-node shell elements having an equivalent thickness. Concrete is idealized using the total strain formulation following the coaxial stress-strain concept (known as the rotating crack model) in which the stress-strain relationship are evaluated in the principal directions of the strain vector. The steel reinforcement mesh is simulated by an embedded grid with equivalent thickness. The stud bolts are taken into account as the horizontal shear transfer mechanism in composite action. In this study, a line interface element with uncoupled stiffness in both the horizontal and vertical directions is employed to represent the shear studs.

3.5 Numerical results

Fig. 13 shows the hysteresis curves for the cycles of 0.005 to 0.04 rad. The dashed and solid lines are the analytical and experimental curves. Correlation between the experimental curves and analytical curves for the composite frame is excellent, with the difference in the stiffness not greater than 10%, and the difference in the maximum strength less than 1.08 % (positive) and 0.52% (negative). In reference to Fig. 13(a), correlation between the test and analysis for the bare steel frame is also good.

3.6 Simulation of fracture

Since the proposed composite structure model is proved to be able to capture the test behavior before fracture occurs, the model is extended to mimic the fracture behavior. Based on the observations from the test and available function in DIANA, a joint model for capturing the effects of weld fracture and subsequent nonlinear response of the connection is proposed.

The joint model consists of 8 rigid links modeled as beam elements and 4 line interface elements. Each pair of rigid links is connected by a 4-node line interface element. The four line interface elements represent top flange, upper part of the web, lower part of the web and bottom flange having corresponding height and out-of-plane thickness. A discrete brittle cracking constitutive relation is adopted for this line interface element. The whole joint model is like a zero-length beam having same dimensions of the adjacent beam.

Prior to fracture, the combination of joint model and adjacent beam elements works like a normal ductile connection. After a fracture occurs, the position where the joint model locates becomes a real hinge.

Each joint model is adopted for eight connections. The connections are separated into two groups, the interior and exterior connections to assign different fracture stresses. The fracture stresses are determined so that the first fracture to the exterior connections and the first fracture to the interior connections would be the same in the test and analysis. The fracture stresses are selected as 325N/mm^2 and 360 N/mm^2 for the exterior and interior connections respectively. Considering the yielding stress of 312N/mm^2 obtained from the associated coupon test for beams, the adopted fracture stresses are within a reasonable range.

Fig. 14 shows the relationship between the shear forces versus the overall drift angle for the composite frame. The analysis results show good correlation between the test and analysis. Note that before the fracture occurred, the structure experienced degradation of stiffness and strength due to cumulative damage at the beam ends. This effect was not able to be simulated by the present model.

3.7 Conclusions

The presence of RC floor slab beneficially increases the stiffness and strength of composite beam while imposes higher strains demanding on the bottom flange of composite beam. That would result in premature failure of composite

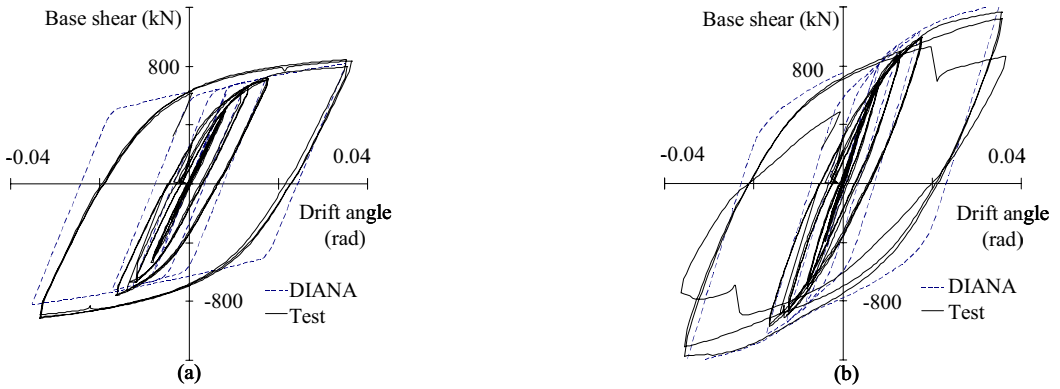

Fig.13 Comparison for global performance of each frame: (a) bare steel frame (to 0.04 rad); (b) composite frame (to 0.04 rad)

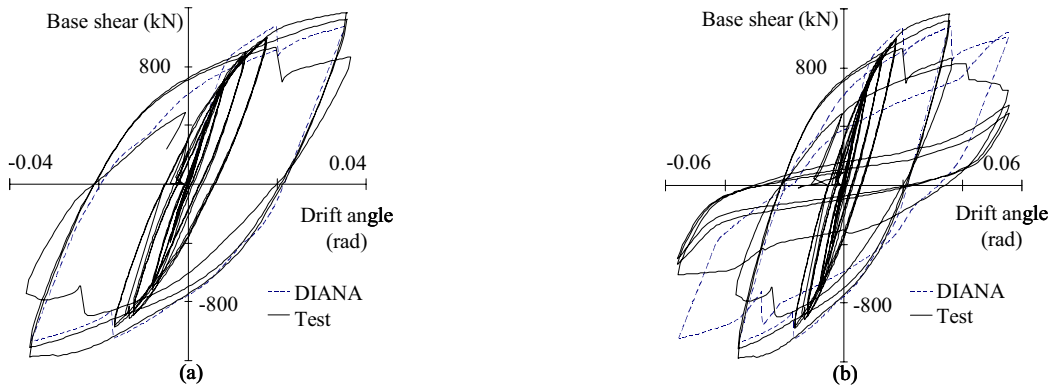

Fig. 14 Comparison for composite frame behavior including fracture (a) to 0.04 rad; (b) to 0.06 rad

beam connections. Even after all connections failed by rupture of bottom flanges and webs, the structure still have certain lateral resistance. The proposed model is capable of capturing the behavior of test structure before and after the connection fracture with acceptable accuracy.

4. Strengthening effects of reinforced concrete columns with polyacetal fiber filaments

In this study, the strengthening effects of reinforced concrete members by applying newly developed polyacetal-fiber (PAF) filaments was investigated. Profitable mechanical properties of the PAF are high tensile strain capacity with adequate strength and stiffness, high shear resistance and light weight. The PAF filaments as a reinforcing material have significant advantages not available from other high strength materials, such as steel and carbon fiber which are currently used for reinforcing of concrete members. These advantages include ability to deform in an acute angle and with a very small radius at room temperature without implement. Moreover The PAF filaments do not need to be impregnated unlike other fibers because of its high tensile strain capacity of 8%. The strengthening effects of concrete members obtained by applying PAF filaments were investigated by conducting lateral loading tests on 5 reinforced concrete columns. The main objectives of the tests were to evaluate the shear capacity determined by bond failure and the ductility of PAF applied columns and to investigate the prediction for both capacities. The test results showed high validity of the PAF filament as a transverse reinforcement, especially for enhancement of the ductility. Meanwhile the shear behavior due to bond failure for columns was modeled by the truss and arch analogy based on the theory of plasticity. The model was verified against the experimental results. It was shown that this model can predict satisfactorily the shear capacity by bond of columns reinforced by not only the PAF filaments, but also steel hoops. A prediction formula for the ductility of columns was proposed by a modification of previous formula by other researchers. The experimental results were found to be in good agreement with the predicted values. This study has been conducted mainly by Cikara IIBOSHI.

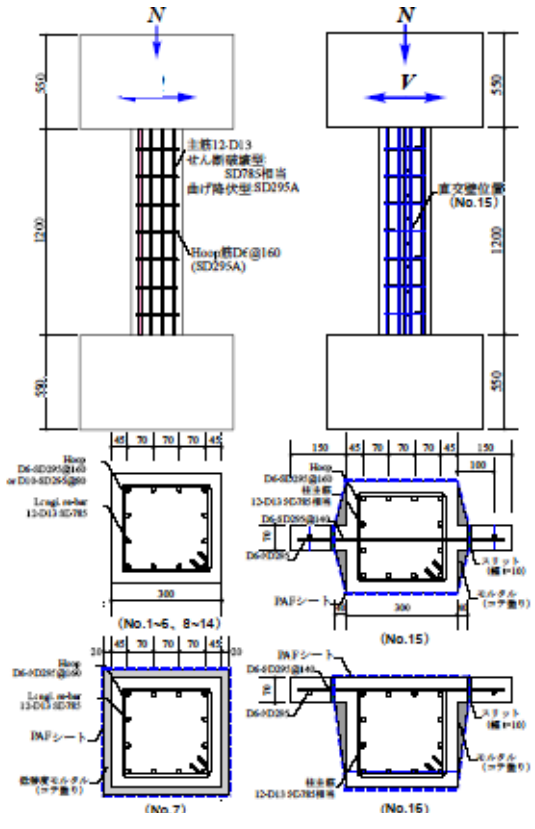

Fig. 15 Test specimen

The mechanical properties of materials are given in Tables 1 and 2. Each column specimen has a square cross section of 300 mm and a effective height of 900 or 1,200 mm as shown in Figure 15. Unit weight of PAF sheet used in the test is 528 g/m^2. Specimens No. 1 ~ 5 and No. 6 ~ 16 have shear span ratio of 1.5 and 2.0, respectively. The major objective of these tests is to investigate the influence of transverse reinforcement with PAF, on shear and ductility for each shear span ratio. The loading of specimens was carried out by means of applying horizontal and axial forces simultaneously. Specimens were loaded statically in the horizontal direction. The axial load was applied constantly throughout the experiment. During the tests, displacements of the loading point and strains in the reinforcing bars and PAF sheet were measured.

From the tests, the following conclusions were obtained:

1) Shear capacity and ductility of existing RC columns can be significantly enhanced by strengthening with PAF sheet.

2) The sheet strengthened column shows the same behavior in both maximum loading capacity and hysteresis loop, as a RC column with equivalent steel reinforcement. Shear strength and ductility of columns confined by PAF can be predicted by proposed equations.

Table 1 Mechanical properties of reinforcement

Materials	No.1~5	No.6~14
	Yield strength (MPa)	
Hoop D6 (SD295A)	360	343
Hoop D10 (SD295A)	----------	347
Longitudinal bar D13 (SD295A)	343	358
Longitudinal bar D13 (equivalent to SD785)	792*2	816

*2 indicates 0.2% off-set point.

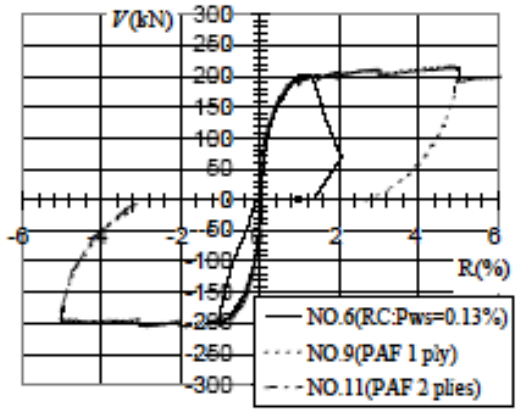

Fig.16 An example of the test results

Table 2 Details of specimens

No.	f'_c (MPa)	N/BDf'_c	M/VD	p_{ws} (%)	p_{wf} (%)	Numbers of PAF sheets plies	Failure mode	Longitudinal bar	Maximum strength (kN)
1	23.6	0.15	1.5	0.13	0.06	1/4*	Shear	equivalent to SD785	*211*
2					0.12	1/2*	Shear	equivalent to SD785	*245*
3					0.24	1	Shear	equivalent to SD785	*238*
4					0.24	1	Flexure	SD295A	*231*
5					0.48	2	Flexure	SD295A	*240*
6	31.4		2.0		------	None	Shear	equivalent to SD785	*202*
7					0.24	Mortar + 1	Shear	equivalent to SD785	*262*
8					0.24	1	Shear	equivalent to SD785	*233*
9					0.24	1	Flexure	SD295A	*216*
10					0.48	2	Shear	equivalent to SD785	*253*
11					0.48	2	Flexure	SD295A	*212*
12				0.59	------	None	Shear	equivalent to SD785	*239*
13		0.30		0.13	0.48	2	Shear	equivalent to SD785	*284*
14					0.48	2	Flexure	SD295A	*266*

3) For strengthened columns with PAF without removal of finished mortar, shear strength and deformability are not affected.

4) Using slits with 90 mm length and 10 mm width, columns with wing walls can be effectively confined by PAF sheets.

5. Contribution of Viscous Force to Horizontal Subgrade Reaction of Piles during Soil Liquefaction

5.1 Objectives

To design pile foundations, the horizontal subgrade reaction of a pile is important factor. Therefore, the horizontal subgrade reaction of piles during soil liquefaction has been studied. Dynamic horizontal subgrade reaction consists of an elastic force component depending on displacement and a viscous force component depending on velocity. The elastic force is generally dominant; therefore, many researchers concentrate on studying p-y curves, where p is soil resistance and y is pile deflection. On the other hands, basic knowledge of the viscous force remains limited. This study investigates the viscous force during soil liquefaction based on pile top vibration tests using a large-scale shear box.

5.2 Pile top vibration tests

The pile top vibration tests were performed at NIED (National Research Institute for Earth Science and Disaster Prevention) in Tsukuba, Japan. The test was jointly conducted by NIED, Tokyo Institute of Technology, Kajima Corp., Taisei Corp., Takenaka Corp., Nippon Steel

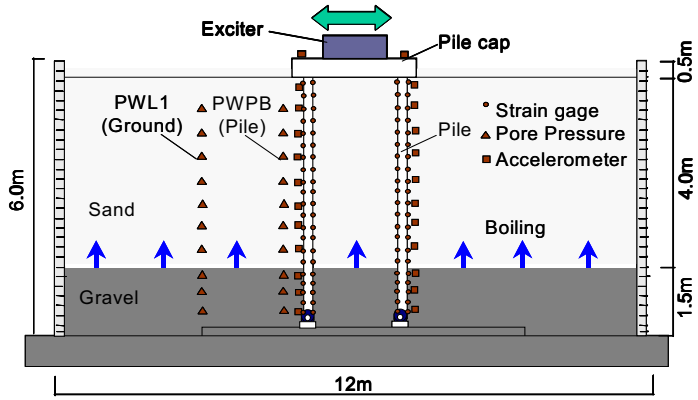

Fig.17 Model setup

Table 3 Test cases

	Pile top vibration test
Ex0	Before boiling
Ex1	1 minute after boiling
Ex2	2.5 minutes after boiling
Ex3	4 minutes after boiling

Corp. and Tokyo Soil Research Corp. The large-scale laminar shear box (6m high, 12m long, and 3.5m wide) including a soil-pile-structure system is diagrammed in Fig. 17. An exciter was mounted on the footing which was supported by 2x2 steel piles. A boiling was performed at GL-4m, the top of the gravel layer. Four cases of pile top vibration tests were carried out before and after the boiling (Table 3). The eccentric moment of the exciter was 98kNm at frequency in the 4- to 10-Hz range.

5.3 Test Results

The relation between the subgrade reaction and the pile displacement, and that between the subgrade reaction and the pile velocity at a height of 4m are shown in Fig. 18. The relation between the pile displacement and the subgrade reaction is an oblate ellipse, while the relation between the pile velocity and the subgrade reaction is an ellipse that approaches a circle in Ex0. This indicates the subgrade reaction depends on the pile displacement in non-liquefied soil. The subgrade reaction is, in contrast, proportional to the pile velocity, indicating that the subgrade reaction depends strongly on the pile velocity in Ex1.

5.4 Elastic force and viscous force

The relation between the pile displacement and the subgrade reaction can be drawn as an inclined elliptical orbit. The inclined ellipse consists of an inclined line component and a non-inclined ellipse component as shown in Fig. 19. The inclined line corresponds to the elastic force (P_d) and the non-inclined ellipse corresponds to the viscous force (P_v). The horizontal subgrade reaction can be expressed by the following equation, according to the Voigt model ,

$$P = \mu \cdot D + \mu' \cdot \frac{dD}{dt} \qquad (1)$$

where D is the pile displacement, μ is the modulus of elasticity and μ' is the coefficient of viscosity. The first term in the right-hand side corresponds to the elastic force and the second term corresponds to the viscous force. μ and μ' can be estimated from the following formula.

$$\mu = \frac{P_1}{D_a} \qquad (2)$$

$$\mu' = \frac{P_2}{\omega \cdot D_a} \qquad (3)$$

where ω is circular frequency, D_a is the amplitude of the pile displacement, P_1 is the subgrade reaction with $D = D_a$, and P_2 is the subgrade reaction with D = zero (Fig.19).

The estimated elastic force and the estimated viscous force are shown in Fig. 20. In Test Ex0, the amplitude of the elastic force is larger than that of the viscous force. On the other hand, the amplitude of the elastic force is far smaller than that of viscous force in Test Ex1.

Figure 21 shows the relation between the excess pore water pressure ratio (u/σ_v') and P_v/P. P_v/P is between 0.1 and 0.2 when the excess pore water pressure ratio is less than 0.5. P_v/P increases with an increase in the excess pore water pressure. When the excess pore water pressure ratio is greater than 0.9, the contribution of the viscous force is greater than 50%.

5.5 Conclusion

The horizontal subgrade reaction of a pile during soil liquefaction was back-calculated based on pile top vibration tests using a large-scale shear box. The subgrade reaction was resolved into an elastic force component and a viscous force component by back analysis using the Voigt model.

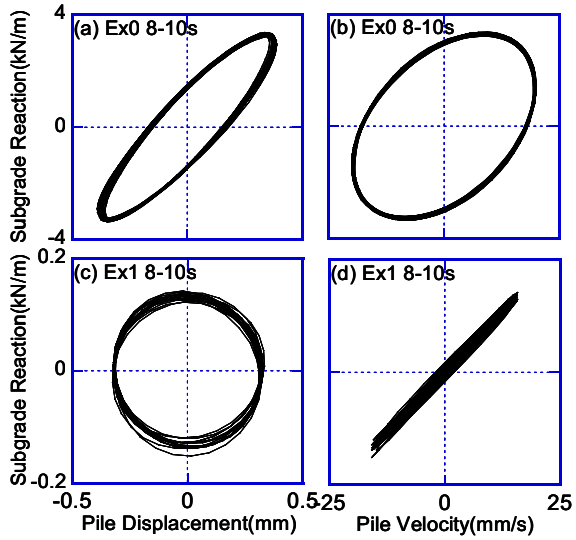

Fig.18 Subgrade reaction with pile displacement and pile velocity at height of 4m

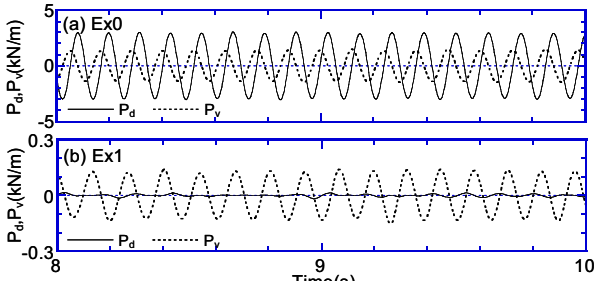

Fig.20 Elastic force and viscous force

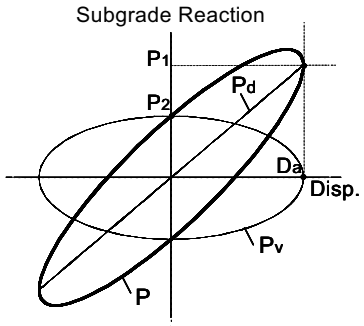

Fig.19 Schematic of relation between subgrade reaction and displacement

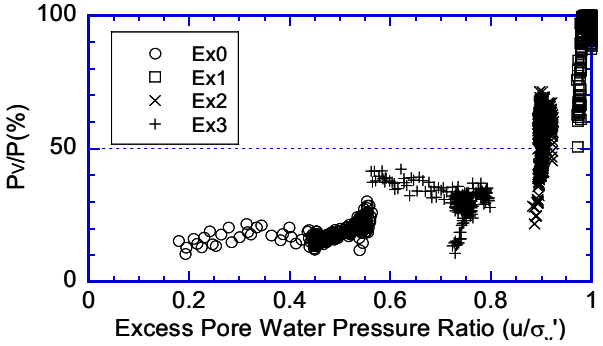

Fig.21 Contribution of viscous force to subgrade reaction

the contribution of the viscous force to the horizontal subgrade reaction increases with an increase in the excess pore water pressure. When the excess pore water pressure ratio is greater than about 0.9, the contribution of the viscous force is greater than 50%.

6. Fragility Curves of Bridge Pier Using Subset Method

6.1 Introduction

Necessity of probabilistic safety assessment (PSA) has been recognized for important facilities such as nuclear power plant in Japan. An effective reliability method is also needed for life cycle cost estimation considering risk that is the product of failure probability and impact of a failure event. In seismic PSA, seismic load and strength of a structure are often estimated separately. Seismic load is modeled based on probabilistic concept, which usually yields to a seismic hazard curve, whereas the structure strength with uncertainties is modeled by a fragility curve.

We propose an efficient method to estimate a fragility curve by using Monte Carlo simulation and limit seismic intensity, which is defined as the minimum amplitude of an input motion causing damage to a structure, in other words, input motion level at where safety factor is 1.0.

If the uncertainty of seismic load is not so large, the tail part of the fragility curve is important to estimate failure probability accurately. For the effective estimation of the tail part, namely low conditional failure probability, we use Subset Simulation proposed by Au and Beck (2002). In this method, samples are generated to search the failure region in each subspace by using Markov Chain Monte Carlo (hereafter referred as MCMC) (Gilks *et al.*, 1996).

The proposed method is verified through a numerical example with simple limit state functions, and then a fragility curve of a steel bridge pier is calculated by the proposed method.

6.2 Estimation of Failure Probability with Limit Seismic Intensity

In general a limit state function defines the failure region as follows,

$$g(S, \boldsymbol{x}_R) < z_0 \tag{1}$$

where, S is a structural parameter with uncertainty, which is sensitive to the limit state, $\boldsymbol{x}_R$ and z_0 are the other uncertain parameters and threshold value to define the failure. The inverse function $R(z_0, \boldsymbol{x}_R)$ is defined to calculate S which satisfy $g(S, \boldsymbol{x}_R)=z_0$, provided $\boldsymbol{x}_R$ and z_0 being given deterministically. Assuming monotonic increase or decrease of function $R(z_0, \boldsymbol{x}_R)$, the failure region can be expressed as follows,

$$R(z_0, \boldsymbol{x}_R)<S, \text{ or } R(z_0, \boldsymbol{x}_R)>S \tag{2}$$

The R is defined as limit intensity. For simplicity, we assume $R<S$ for failure zone in following discussion.

Assuming independence between S and the other parameters, the probability density function (hereafter referred as *f* or *pdf*) of the parameters is expressed by,

$$f(S, \boldsymbol{x}_R) = f_S(S) f_{\boldsymbol{x}_R}(\boldsymbol{x}_R) \tag{3}$$

The failure probability can be obtained as follows,

$$P_f = \int_{g<z_0} f(S, \boldsymbol{x}_R) dS d\boldsymbol{x}_R = \int_{R<S} f_S(S) f_{\boldsymbol{x}_R}(\boldsymbol{x}_R) dS d\boldsymbol{x}_R = \int \left(\int_{R<S} f_S(S) dS \right) f_{\boldsymbol{x}_R}(\boldsymbol{x}_R) d\boldsymbol{x}_R$$
$$= \int \left(\int_{R(z_0, \boldsymbol{x}_R)}^{\infty} f_S(S) dS \right) f_{\boldsymbol{x}_R}(\boldsymbol{x}_R) d\boldsymbol{x}_R = \int \{1 - F_S(R(z_0, \boldsymbol{x}_R))\} f_{\boldsymbol{x}_R}(\boldsymbol{x}_R) d\boldsymbol{x}_R \tag{4}$$

The failure probability for S conditioned by $R<S$ can be expressed.

$$F_R(S) = \int_{R<S} f(S, x_R) dx_R = \int U(S - R(z_0, x_R)) f_{x_R}(x_R) dx_R \tag{5}$$

Here, U(x) is step function, =1 when x is non-negative, 0 when x is negative. It corresponds to a so-called fragility curve used in seismic PSA, when S is seismic intensity such as SI, PGA, or PGV.

In this study, Monte Carlo simulation is used for the integration of Eq.(4) or (5). The probability density function of xR is approximated by using samples generated according to the f(xR) and Dirac's delta function.

$$f_{x_R}(x_R) = \frac{1}{n} \sum_{j=1}^{n} \delta(x_R - x_R^{(j)}) \tag{6}$$

Substituting Eq.(6) into Eq.(4), we obtain Eq.(7), which calculates the failure probability. In same way, Eq.(8) is derived to estimate fragility curve.

$$P_f = \frac{1}{n} \sum_{j=1}^{n} \left(1 - F_S\left(R(z_0, \boldsymbol{x}_R^{(j)})\right)\right) \tag{7}$$

$$F_R(S) = \frac{1}{n} \sum_{j=1}^{n} U\left(S - R(z_0, x_R^{(j)})\right) \tag{8}$$

A fragility curve can be defined as conditional failure probability, provided seismic intensity (PGA). An approach to estimate a fragility curve is to perform MCS based on Eq.(1). Figure 22 shows an illustration of MCS for given PGA. This is a simple way to estimate a fragility curve but we need to perform MCS many times. The proposed method is illustrated in Figure 23. In this method, for each generated $\boldsymbol{x}_R^{(j)}$ by a single MCS the inverse function $R(z_0, \boldsymbol{x}_R^{(j)})$ is calculated and then fragility curve is obtained by using Eq.(8). Although the estimation of $R(z_0, \boldsymbol{x}_R^{(j)})$ needs longer computation time than to evaluate the ordinary limit state value $g(S, \boldsymbol{x}_R)$, the proposed method is

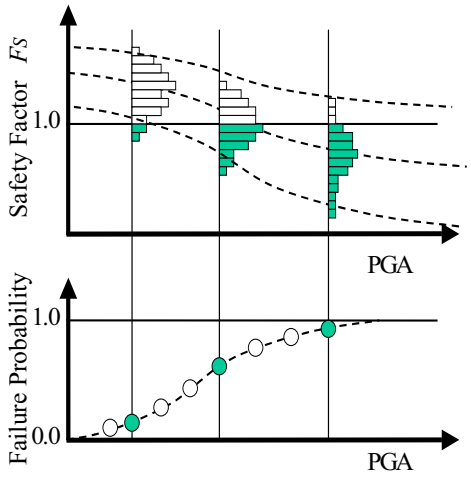

Fig. 22 Illustration for Evaluating a Fragility Curve in General

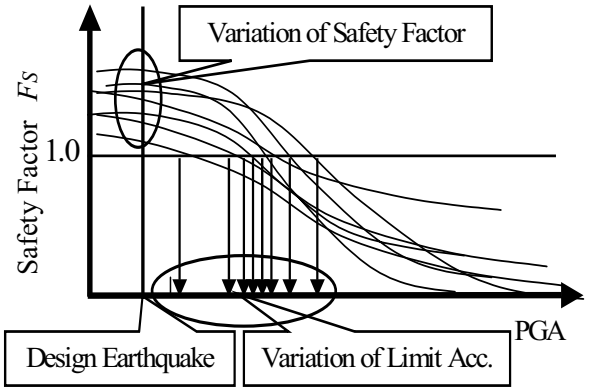

Fig. 23 Estimated fragility curve (*cdf*) and *pdf* of the generated samples

more efficient in most cases because a fragility curve can be obtained by the single MCS.

6.3 Outline of Subset Simulation

Procedure of Subset Simulation

The procedure of Subset Simulation (Au and Beck, 2002) is summarized as follows.

(a) Generate n_t samples according to *pdf*(x) and calculate limit state function value.

(b) Sort the samples according to the order of its value such as z_1, z_2,..., z_n in which z_1 is the smallest value. The subspace F_{k+1} is defined with the following equation for given n_s.

$$F_{k+1} = \{\boldsymbol{x} | z(\boldsymbol{x}) < C_{k+1}\}, \quad C_{k+1} = \frac{z_{n_S} + z_{n_S+1}}{2} \tag{9}$$

(c)Generate n_t samples in the subspace with MCMC (Gilks *et al*, 1996).

(d)If the number of samples reaches failure zone becomes large enough, then stop the calculation, otherwise go back to the step 2.

The failure probability can be calculated with the number of samples in failure zone n_f in subset k,

$$P(z<0) = \left(\frac{n_s}{n_t}\right)^k \frac{n_f}{n_t} \tag{10}$$

MCMC with uniform distribution

The outline of Markov Chain Monte Carlo is described briefly. Samples according to arbitrary target distribution $\pi(x)$ can be generated by MCMC.

(a)Set an arbitrary initial value x_0 and k=0 (k being a counter)

(b)Generate x' according to the proposal distribution $q(x'|x_k)$

(c)Calculate the acceptance ratio

$$\alpha(x_k, x') = \min\left\{1, \frac{\pi(x')q(x_k|x')}{\pi(x_k)q(x'|x_k)}\right\} \tag{11}$$

(d)x' is accepted as x_k with probability α, otherwise x_k becomes x_{k+1}

(e)$k = k+1$, go to step 2

In our method, the every variable is firstly generated using uniform distribution which is denoted as $\boldsymbol{u}$. The $\boldsymbol{u}$ is then transformed into any type of distribution with cumulative distribution function (hereafter referred as *cdf*)

$\Phi(x)$

$$\boldsymbol{x} = \Phi^{-1}(\boldsymbol{u}) \tag{12}$$

The proposal density function $q(x'|x_k)$ can be any arbitrary function. In our study, it is assumed to be a uniform distribution with mean x_{k+1} as defined by

$$q(u'/u_k) = \begin{cases} \dfrac{1}{2a}; & u_k - a < u' < u_k + a \\ 0; & \text{otherwise} \end{cases} \tag{13}$$

The *pdf* of subset F_i is given as follows,

$$pdf(x/F_i) = \frac{pdf(x)I_{Fi}(x)}{P(F_i)} \tag{14}$$

in which $I_{Fi}(x)$ is indicator function, =1 when x is in subset F_i, otherwise =0. Defining $I_{(0,1)}(u)$ as uniform distribution in region (0, 1), Eq.(7) can be written,

$$pdf(u/F_i) = \frac{pdf(u)I_{Fi}(u)}{P(F_i)} = \frac{I_{(0,1)}(u)I_{Fi}(u)}{P(F_i)} \tag{15}$$

In this study, the uniform distribution in Eq.(13) is used as the proposal distribution, therefore the acceptance ratio can be simplified as follows.

$$\begin{aligned}\alpha(x_k, x') &= \min\left\{1, \frac{\pi(x')q(x_k|x')}{\pi(x_k)q(x'|x_k)}\right\} = \min\left\{1, \frac{P(F_i)I_{(0,1)}(u')I_{Fi}(u')2a}{P(F_i)I_{(0,1)}(u_k)I_{Fi}(u_k)2a}\right\} \\ &= \min\left\{1, I_{(0,1)}(u')I_{Fi}(u')\right\}\end{aligned} \tag{16}$$

In the case of high dimensional problem, it is not efficient to update all variables at the same time because the acceptance ratio becomes very low. In the algorithm called single-component Metropolis-Hastings (Gilks *et al*, 1996), each variable is updated separately. Eq.(16) contains two kinds of criteria $I_{(0,1)}(u')$ and $I_{Fi}(u')$. For $I_{(0,1)}(u')$, the procedure of single-component Metropolis-Hastings is applied. The parameter "a" has a strong influence on the efficiency of the simulation, several values of "a" are used sequentially in the simulation.

6.4 Numerical Example of Push Over Analyses

(1)Estimation of Fragility Curve of an Existing Steel Pier of Bridge

We apply the proposed methodology to an actual steel frame bridge shown in Figure 24 and calculate a fragility curve of this structure in which we consider several uncertainties of the structural parameters including the

mass of upper structure, yield stress, thickness of plate and so on. We divide the bridge into 6 parts and consider a yield stress for each part. Limit acceleration (PGA, peak ground acceleration) is used as limit seismic intensity. Though three limit states, bending, shear and deformation, are considered in an actual design, we consider only bending mode for simplicity. We followed the ordinary design procedure of a bridge pier in Japan (Design of Highway Bridge Foundations in Japan, 2003) which is consisted of the following three steps: 1) Perform two-dimensional push over analysis and obtain relation between applied load and bending deformation. 2) Estimate applied load to cause failure based on energy conservation principle and limit stage design point. 3) Limit acceleration is calculated based on the applied load, the predominant period and weight of the bridge.

Based on the energy conservation principle we calculate seismic load to cause the structure failure, however, it has been shown that this principle tends to overrate the maximum response displacement for steel structures in comparison with the result of nonlinear dynamic analysis. Some researchers study this reason and show that it is based on the difficulty to define yield point and damping characteristic of steel structures. Because this overrating brings designed structures in the safer region, we use this principle even though there are still controversial opinions. We, however, take this uncertainty into account to calculate the fragility curve.

Basic parameters of the Pier Model

Young's Modulus of steel and concrete are 2.0×10^{8}(kN/m^2)and 2.0×10^{7}(kN/m^2), respectively. Damping constant of them are 0.03 and 0.02. The caisson foundation is modeled by a mass with rotation and horizontal springs. Mass of upper structure is loaded at node 2, 6, 10, 15 (Figure 24), and they are 21551.18(kN), 915.32(kN), 985.88(kN), 19763.66(kN), respectively. Stress strain relationship of steel is assumed to be expressed by the Bi-linear model and we calculate M-ϕ relation of the box type steel pier element to obtain equivalent bending rigidity of beam element based on the Guide line of anti-seismic reinforcement for existing steel bridges (Hanshin Expressway Public Corporation, 1997). Furthermore we take into corrosion effect account on the reduction of thickness of steel plate used for bridge pier.

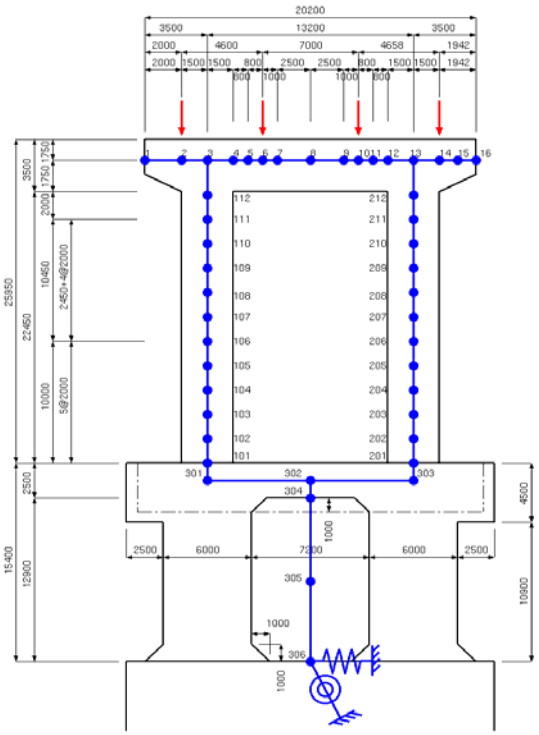

Fig.24 The model of steel bridge pier

Uncertainties to be considered

(a)Mass of upper structures

From observation data for several bridges, we assume the ratio between observed value and design value is

Table 4 Uncertainties Considered in the Example

Uncertainties		Mean(μ)	Standard Deviation(σ)	C.O.V	Distribution
Mass of upper structure observed value / design value		1.03	0.02	0.019	Normal
Strength of component	Yield stress *Mm* observed value / design value	1.15	0.1265	0.11	Lognormal
	Thickness of plate *Fm* observed value / design value	1.00	0.05	0.05	Normal
Ground factor	Soil Spring	1.0×Calc.	0.1μ	0.1	Normal

distributed as normal distribution with the mean 1.03 and standard deviation 0.02.

(b)Strength of component

・Yield stress: We define $Mm=\sigma y/Fy$. σy is observed yield stress of actual structures and Fy is designed value. From 1122 data, we assume Mm is distributed as lognormal distribution with the mean 1.15 and c.o.v. 0.11.

・Thickness of steel plate: We define $Fm=Sm/Sn$. Sm is observed cross-section factor of actual structures and Sn is designed value. From data, we assume Fm is distributed as normal distribution whit the mean 1.00 and c.o.v. 0.05.

(c)Foundation part

Because variation of soil parameters is not easy to evaluate for defining equivalent spring constants of foundation model we assume soil spring factor is distributed as normal distribution with c.o.v. 0.1.

(d)Energy conservation principle

The energy conservation principle tends to overrate the maximum response displacement for steel structures. From investigation (by Kitahara, 2001), we assume that the ratio between maximum response displacement derived by this principle and that obtained by nonlinear dynamic analysis is 1.42 (mean) and its c.o.v. is 0.329.

(e)Corrosion

10 years have passed since the target bridge was constructed. From observation data, we assume the mean decrement of the thickness of plate caused by corrosion is 0.255mm and its standard deviation is 0.4.

(f)Ultimate strength

Ultimate strength is assumed to be distributed. From results of buckling experiment, we assume ultimate strength is distributed as normal distribution, c.o.v. 0.05.

Criterions

Because there are many elements in the bridge pier model we define the critical condition (failure) of the pier as one of element's curvatures exceeds the threshold value. At this time, the displacement of top of the pier (node 8 in Figure 24) is defined as the final horizontal displacement and the horizontal load as final horizontal load to cause failure. Using them, we estimate the applied load to cause failure based on energy conservation principle and we obtain limit acceleration dividing this lord by the mass of superstructure.

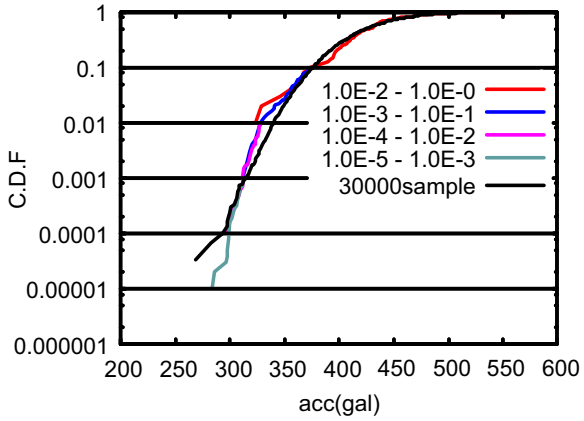

Fig.25 Estimated fragility curve (cdf) (9 uncertainties)

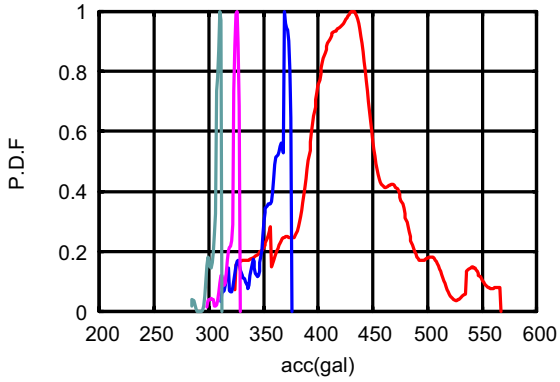

Fig.26 Distribution of samples (pdf)

Numerical Example

In this case, we consider 9 uncertainties as summarized in Table 4 and assume ultimate strain of $10\varepsilon y$ (εy is yield strain) as critical condition of pier (Guide line of anti-seismic reinforcement for existing steel bridges, 1997). So the curvature defined when strain exceeds $10\varepsilon y$ is threshold value. First, we perform the ordinary MCS to obtain the fragility curve with 30,000 samples. Then we estimate the fragility curve by Subset Simulation with 100 samples in each subspace. The computation time is less than 1/70 of ordinary MCS. We adopt the parameter n_f=100, n_s=10, and the ten types of proposal density function using different values of parameter "a". The obtained fragility curves are shown in Figure 25. An accuracy of MCS is represented by c.o.v. δ.When the failure probability P_F is small, the number of samples $N\delta$ required to achieve given δ is expressed by,

$$N_\delta = \frac{1-P_F}{P_F\delta^2} \approx \frac{1}{P_F\delta^2} \qquad (18)$$

As we use 30,000 samples for ordinary MCS, we can estimate $P_F=10^{-3}$ with an accuracy of δ=0.2. In Figure 25, the fragility curve obtained by using Subset Simulation agrees well with the fragility curve obtained by the

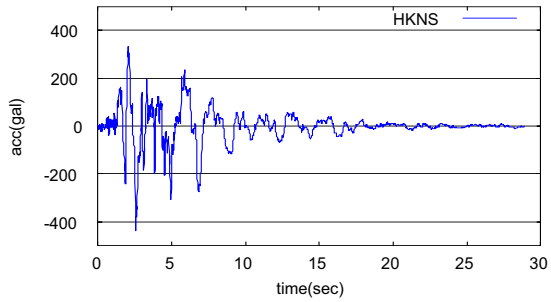

a) Time history of acceleration observed at Higashi Kobe (NS)

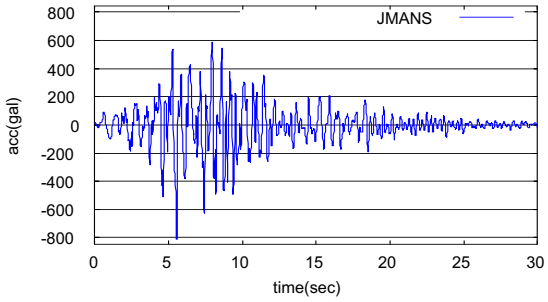

b) Time history of acceleration observed at JMA Kobe (NS)

Fig.27 Input motions

ordinary MCS up to the level of 10^{-3}. Additionally, the distribution of the generated samples (pdf) is shown in Figure 26. This result shows that the samples are well generated from the tail part of the former subset.

6.5 Comparison of Fragility Curves Obtained by Pushover and Dynamic Analyses-

Considering an actual steel frame bridge shown in Figure 24 and uncertainties in Table 4, we estimate fragility curves by dynamic analysis using two different input motions which are shown in Figure 27, a)Higashi Kobe (NS), b)JMA Kobe (NS), which are observed during the 1995 Hyogoken Nambu earthquake in Japan. We use Rayleigh damping for nonlinear structural analysis assuming 0.5% damping constant for first and second mode. We assume bi-linear hysteric characteristics for each beam element to express nonlinear M-ϕ relationship. We conduct dynamic analysis for each sample bridge pier and calculate the limit acceleration by changing peak amplitude of acceleration time history. Estimated fragility curves are shown in Figure 28. It should be noticed that two fragility curves obtained by dynamic analysis are different each other although the process to obtain the limit acceleration are same for both cases. This causes by the difference of time history shape which is strongly controlled by the phase spectrum. In this figure, a fragility curve estimated by pushover analysis based on energy conservation principle is also shown. To obtain this curve we consider the uncertainties not only given in Table 4 but uncertainty of the energy conservation principle. We can see fragility curves obtained by dynamic analysis are on the right side of that obtained by push over analysis. This tendency is consistent with the Kitahara's finding that the energy conservation principle tends to overestimate an ultimate displacement of steel bridge piers about 1.42

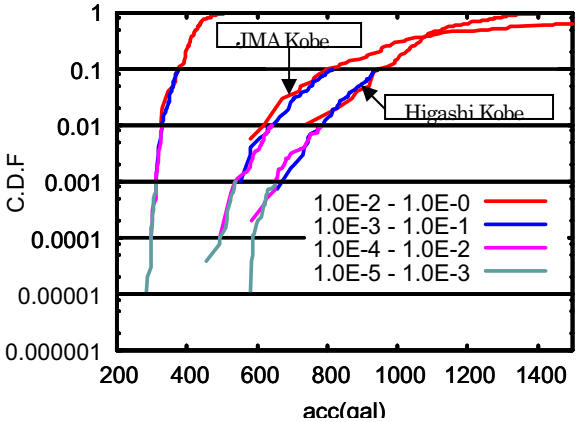

Fig.28 Estimated fragility curves (cdf)

times with standard deviation of 0.467 of which data distribution width is from 0.7 to 2.8 times. (Kitahara 2001).

6.6 Conclusion

An efficient method based on MCS was proposed to estimate a fragility curve. The concept of Subset Simulation was adopted when the tail part of the fragility curve becomes important. Since efficiency of MCMC plays an important role in the Subset Simulation several method were proposed to improve the efficiency by using such as hit and run algorithm (Gilks *et al*, 1996). We applied proposed method to actual bridge piers considering several uncertainties of the structure. The efficiency of this method was demonstrated by numerical examples.

Acknowledgements

We use data of K-NET, KiK-net, PARI strong motion network, and CEORKA.

References

Au, S-K and Beck, J. L. (2002): Application of Subset

Simulation to Seismic Risk Analysis, 15th ASCE Engineering Mechanics

Furumura, T., B. L. N. Kennett, and K. Koketsu. (2003): Visualization of 3D wave propagation from the 2000 Tottori-ken Seibu, Japan, Earthquake: Observation and numerical simulation, Bull. Seism. Soc. Am., 93, pp.870-881.

Gilks, W.R., Richardson, S., Spiegelhalter, D.J. (1996): Markov chain Monte Carlo in practice, Chapman & Hall.

Hanshin Expressway Public Corporation. (1997): Guide line of anti-seismic reinforcement for existing steel bridges.

Kagawa, T., B. Zhao, K. Miyakoshi, and T. Akazawa. (2002): A procedure of modeling basin structure used for strong ground motion evaluation from any amount of given information -Case study for the Osaka basin-, Proc. 11th Japan earthquake engineering symposium, pp.497-500, (in Japanese).

Kitahara, T. (2001): Aseismic design method considering periodic and phase characteristics of earthquake motions, doctoral dissertation of Nagoya University

Nakamura, M., H. Watanabe, T. Konomi, S. Kimura, and K. Miura. (1997): Characteristics activities of subcrustal earthquakes along the outer zone of southwestern Japan, Annuals of Disas. Prev. Res. Inst., Kyoto Univ., Vol.40 (B-1), pp.1-20, (in Japanese).

Public Works Research Institute. (2003): Design of Highway Bridge Foundations in Japan, Foundation Engineering Research Team, Structures Research Group.

Sato, T., Y. Murono and A. Nishimura. (2000): Empilical modeling of phase spectrum of earthquake motion, Journal of the Japan Society of Civil Engineers, No.640,I-50, pp.119-130.

Yamada, N. and T. Iwata. (2004): Long-period ground motion simulation in Kinki area, Annuals of Disas. Prev. Res. Inst., Kyoto Univ., Vol.47 C, pp.149-155,.

Zhao, D., A. Hasegawa, and H. Kanamori. (1994): Deep structure of Japan subduction zone as derived from local, regional, and teleseismic events, J. Geophys. Res., 99, pp.22313-22329.

多次元評価指標の統合化による都市施設地震脆弱性診手法の高度化

佐藤忠信・田中仁史・中島正愛・岩田知孝・
吹田啓一郎・澤田純男・田村修次・
本田利器・山田伸之*

*京都大学防災研究所

要旨

都市域に存在する多くの構造物の地震時における脆弱性を合理的に評価するためには，構造物の共用期間，地震時に作用する外力，それに起因する被害コストや復旧にかかるコスト，さらには補強や維持管理にかかるコストも考慮に入れる必要があると考えられる．本研究では，このような点に鑑み，シナリオ地震による強震動予測や，RC床板を含む鉄骨フレームの実物大実験，新たに開発されたアセタール樹脂繊維 (PAF)によって補強されたコンクリート部材の変形特性，液状化地盤内の基礎杭にはたらく水平地盤反力の特性，さらに，サブセット法とマルコフ・モンテカルロ法に基づいてフラジリティ曲線を求めるための効率的な方法に関する統合的な研究を実施した．

キーワード：強震動予測，長周期地震動，耐震補強，実大実験，ライフサイクルコスト，フラジリティ曲線